High-Fidelity Control of a ^{13}C Nuclear Spin Coupled to a Tin-Vacancy Center in Diamond

Jeremias Resch,[1,*] Ioannis Karapatzakis,[1,*] Mohamed Elshorbagy,[1] Marcel Schrodin,[1] Philipp Fuchs,[2] Philipp Graßhoff,[3] Luis Kussi,[1] Christoph Sürgers,[1] Cyril Popov,[3] Christoph Becher,[2] Wolfgang Wernsdorfer,[1,4] and David Hunger[1,4,†]

[1]*Physikalisches Institut, Karlsruhe Institute of Technology, Kaiserstraße 12, 76131 Karlsruhe, Germany*
[2]*Department of Physics, Saarland University, Campus E2 6, 66123 Saarbrücken, Germany*
[3]*Institute of Nanostructure Technologies and Analytics (INA), Center for Interdisciplinary Nanostructure Science and Technology (CINSaT), University of Kassel, Heinrich-Plett-Straße 40, 34132 Kassel, Germany*
[4]*Institute for Quantum Materials and Technologies, Karlsruhe Institute of Technology, Kaiserstraße 12, 76131 Karlsruhe, Germany*

(Received 18 August 2025; accepted 9 February 2026; published 19 March 2026)

Nuclear spins near group-IV defects in diamond are promising candidates for quantum memories in quantum network applications. Here, we demonstrate high-fidelity control of a single ^{13}C nuclear spin coupled to a tin-vacancy center in diamond. We perform a combination of optical and microwave pumping to achieve initialization into a combined electronuclear spin state with a fidelity of 99.74(3)%. Harnessing a superconducting waveguide for radio-frequency driving, we demonstrate precise nuclear-spin control: Ramsey measurements reveal a coherence time of $T_2^* = 1.5(1)$ ms, and we use dynamical decoupling to extend it to 1.35(3) s. We perform randomized benchmarking, yielding a single-qubit gate fidelity of 99.92(1)%. This demonstrates a coherent spin-photon system with promising properties for quantum network nodes.

DOI: 10.1103/bmc6-qvwq

Subject Areas: Condensed Matter Physics, Quantum Physics, Quantum Information

I. INTRODUCTION

Nuclear spins in the vicinity of optically addressable spin defects in diamond are promising candidates for spin-photon interfaces, which represent an essential building block for the implementation of quantum networks [1]. It has been shown that group-IV centers yield coherent optical transitions with minimal spectral diffusion [2–6], offer long-lived electron spins that can be driven coherently [6–10], and give access to nuclear spins as quantum memories, harnessing either the defect-centered ^{29}Si [8], ^{73}Ge [11], or ^{117}Sn [12] spins or neighboring ^{13}C nuclei [13–16].

The tin-vacancy (SnV) center has recently gained attention due to its bright optical transition [4], long spin lifetime at elevated temperature, and access to fast spin manipulation in a strained diamond lattice [6,9,10]. In addition, single-shot readout of the electron spin has been demonstrated [17]. Although the coherence of the electron spin could be extended to 10 ms [6], this is still not sufficient for building quantum networks. Recent work on SiV and GeV centers have shown the possibility to extend the coherence time of a single proximal ^{13}C nuclear spin up to the seconds range [8,14]. Also, protocols have been demonstrated to control weakly coupled ^{13}C spins with group-IV defects and their electron spin 1/2 [15,16]. Still, using such spins as quantum memories requires high-fidelity manipulation, which so far has been reported only for NV centers [18].

In this work, we demonstrate high-fidelity control of a single strongly coupled ^{13}C nuclear spin located near a negatively charged SnV center. We investigate the hyperfine interaction using optically detected magnetic resonance (ODMR) and initialize the nuclear spin into a selectively chosen spin state with a fidelity exceeding 99% by employing a combination of optical and microwave (MW) pumping. Using a superconducting coplanar waveguide, we demonstrate direct radio-frequency (rf) control of the nuclear spin with negligible heating, enabling high-fidelity coherent manipulation. Using Carr-Purcell-Meiboom-Gill (CPMG) decoupling sequences, we extend the nuclear-spin coherence time to up to 1.35(3) s, with potential for further extension. Finally, we determine a single-qubit gate fidelity of 99.92(1)% through randomized benchmarking. In addition

[*]These authors contributed equally to this work.
[†]Contact author: david.hunger@kit.edu

to the beneficial spin properties, we observe excellent optical coherence and spectral stability of the optical transition, which in combination achieves key requirements for a quantum network node.

II. THE SETUP

This study uses an electronic grade diamond membrane with a natural abundance of 1.1% ^{13}C nuclear spins. For coherent microwave and radio-frequency spin control, a coplanar waveguide (CPW) made out of niobium with a 5 μm gap at the end of a constriction is fabricated on the diamond by optical lithography and subsequent electron beam evaporation of niobium. For further details on the waveguide fabrication, see Ref. [6]. The sample is mounted in a home-built dilution cryostat with a base temperature of 50 mK and is surrounded by a 3D vector magnet. Optical access is given through an objective and optical windows toward a confocal microscope setup.

Figure 1(a) shows a simplified energy-level scheme and the atomic defect structure of the SnV center [4]. Only the lower orbital branch of the ground (excited) state (GS) [(ES)] is shown. The red sphere represents the tin ion on the interstitial site between two vacancies, which are depicted as gray spheres. A ^{13}C nuclear spin is highlighted by a blue sphere in the surrounding carbon lattice.

We probe the system with a narrow-band laser resonantly driving the spin-conserving A1 transition [see Fig. 1(a)] and detect the phonon-sideband (PSB) fluorescence. Using sufficiently low powers for resonant excitation ($p_{\mathrm{PLE}} = 0.6$ nW $\approx p_{\mathrm{sat}}/50$) enables the optical line to remain stable for hours, maintaining a narrow linewidth and a stable charge state; see Fig. 1(b). A Lorentzian fit to a single measurement yields a close to Fourier-limited linewidth of 34(4) MHz compared to a linewidth of the averaged spectrum of 36.6(1) MHz (see Fig. 8 in Appendix A 1). The small broadening of the hour-long averaged spectrum compared to the single line sweep shows the negligible spectral diffusion present. In the rare occasion of a charge transition, a weak repump pulse of a few nanowatt power with a 532 nm laser is used. This allows for a simple measurement sequence without the need for frequent repumping [9,19] or postselection [17,20]. Such high stability is a beneficial ingredient for spin-photon entanglement and quantum network applications.

The electronic spin structure of the SnV center in a magnetic field is discussed in detail in the literature [6,9,10,21]. By applying an external magnetic field along

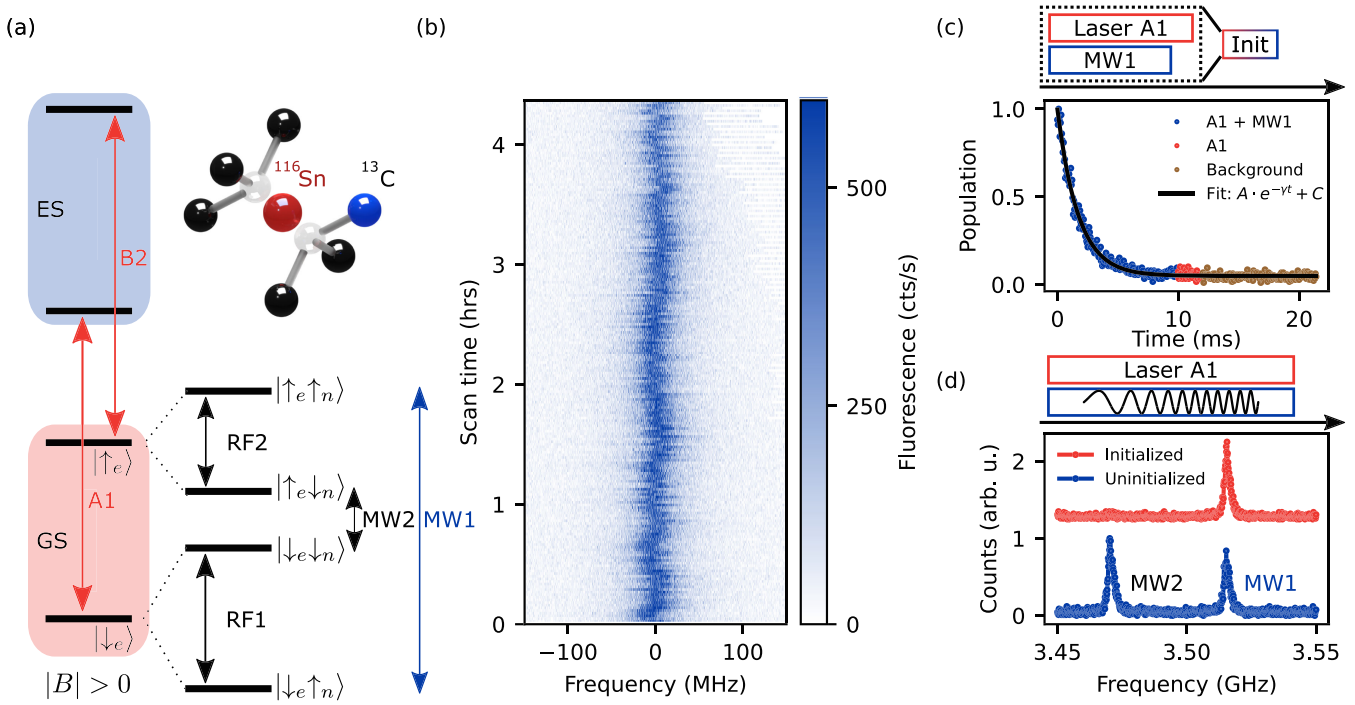

FIG. 1. (a) Energy-level scheme of the SnV center coupled to a proximal ^{13}C nuclear spin in a nonzero magnetic field. The electron-spin levels $|\downarrow_e\rangle, |\uparrow_e\rangle$ are split by the electronic Zeeman effect. Coupling to the ^{13}C nuclear spin leads to a further splitting into four sublevels. (b) Photoluminescence excitation measurement performed at zero magnetic field. A single sweep linewidth yields a FWHM of 34(4) MHz. Repeated scans show the absence of spectral jumps and charge state switching. (c) Initialization into the state $|\uparrow_e\downarrow_n\rangle$ by driving the optical transition A1 and the microwave transition MW1 for 10 ms. A fit yields an initialization fidelity of $F_{\mathrm{init}} = 99.74(3)\%$. (d) ODMR measurement showing the hyperfine splitting of the electron-spin transition due to the ^{13}C nuclear spin, yielding two microwave transitions MW1 and MW2 (blue data), which can be attributed to the two rf transitions shown in (a). After initialization into the state $|\uparrow_e\uparrow_n\rangle$ by applying an initialization with MW2 and A1, only one resonance remains (red data).

the quantization axis of the SnV center, the electronic sublevels are split into the two $\{|\downarrow_e\rangle, |\uparrow_e\rangle\}$ spin levels as shown in Fig. 1(a). A strong coupling of the electron spin to a proximal nuclear spin with states $|\downarrow_n\rangle$ or $|\uparrow_n\rangle$ leads to a further splitting of these levels. This results in a total of four levels in ascending order $\{|\downarrow_e\uparrow_n\rangle, |\downarrow_e\downarrow_n\rangle, |\uparrow_e\downarrow_n\rangle, |\uparrow_e\uparrow_n\rangle\}$ in the electronic ground state. The depiction of the excited state is simplified to just two levels, as only the spin-conserving optical transitions A1 and B2 are driven by the applied laser pulses. There are a total of two nuclear-spin-conserving microwave transitions MW1 and MW2, which drive the electron spin, and two electron-spin-conserving radio-frequency transitions RF1 and RF2 driving the nuclear spin. Figure 1(d) shows a typical ODMR measurement, where the frequency of the microwave is swept in a chirp over the expected range of the electron-spin resonance, while pumping the spin-conserving optical transition A1 and collecting the PSB fluorescence. The precise electron-spin resonance frequencies can be obtained for arbitrary magnetic fields using the Hamiltonian parameters introduced in earlier work [6]. Fitting the optical transitions to the Hamiltonian, we obtain a low strain value corresponding to a frequency splitting of 41.3(8) GHz for the ground state and 66(3) GHz for the excited state (see Appendix A 2 for more details).

III. SPIN INITIALIZATION

To use the nuclear spin as a qubit, it must first be initialized into one of its sublevels. This can, for example, be achieved via the implementation of a SWAP gate [14], using resonances in spin echo sequences [13], or using Hartmann-Hahn conditions [22]. However, due to the low electron Rabi frequency of low-strain SnV centers under magnetic fields aligned with the SnV quantization axis (see Appendix C 5), we opt for an alternative approach based on optical pumping. This technique involves the simultaneous application of one of the microwave transitions and one of the spin-conserving optical transitions, e.g., MW1 in combination with A1 for an initialization into $|\uparrow_e\downarrow_n\rangle$. Figure 1(c) illustrates a representative initialization sequence, in which transition A1 is optically pumped while MW1 is applied at a low power of −16 dBm. The nuclear spin flips randomly, eventually occupying the state $|\uparrow_e\downarrow_n\rangle$, which is off resonant with both the laser and microwave fields and, thus, constitutes a dark state. This scheme results in an exponential decay of the PSB fluorescence signal. To infer the level of laser-induced background fluorescence, a short (ms) laser-only pulse is typically appended at the end of the sequence. Fitting the fluorescence decay to an exponential function with amplitude and offset, we extract the initialization fidelity as $F_{\text{init}} = 99.74(3)\%$ by subtracting the offset from the amplitude and normalizing to the total signal (see Appendix B 1). Owing to the high cyclicity of this process, initialization requires about 5–10 ms, depending on the applied optical and microwave power. We find a pure electron cyclicity of $\Lambda_e \sim 6000$ (see Appendix B 2).

Using an analogous pumping scheme but applying the transition MW2, one can initialize in the $|\uparrow_e\uparrow_n\rangle$ state, leaving only MW1 as a bright transition in the ODMR measurement as shown in Fig. 1(d).

ODMR measurements reveal a splitting of 44.91(3) MHz [see Fig. 1(d)], which indicates a proximal nuclear spin [23], most probably one of the next neighbors as indicated in Fig. 1(a). The exact positions of the radio-frequency transitions RF1 and RF2 were determined by an optically detected nuclear resonance (ODNR) measurement by continuously pumping the corresponding optical transition B2 or A1 and driving continuously one of the microwave transitions while chirping the radio frequency (see Fig. 5 in Appendix A 2). We note that, due to the close proximity of the nuclear spin, a significant Fermi contact interaction is present, and it is not possible to extract the parallel and perpendicular coupling parameters of the interaction using the secular approximation [14].

IV. COHERENT SPIN CONTROL

The ability to initialize the nuclear spin and knowledge of its transition frequency allows for coherent control. We use a superconducting waveguide comparable to the one used for electron-spin manipulation in Ref. [6]. Figure 2(a) shows a Rabi chevron pattern around the center frequency 20.998 MHz. This is measured by initializing into the state $|\uparrow_e\uparrow_n\rangle$ via MW2 and coupling to the bright state $|\uparrow_e\downarrow_n\rangle$ by rf pulses at frequency RF2 of varying duration and detuning under a magnetic field of 60 mT along the SnV axis. With an rf input power of only 10 dBm, a Rabi frequency of 12.93(7) kHz is achieved. The observed nuclear Rabi frequency is slightly enhanced by a factor of 2.06(1) compared to a free ^{13}C nuclear spin due to the coupling to the nearby electron spin. For further details on the microwave calibration and estimation of the enhancement, see Appendixes A 3 and C 1. An external magnetic field of 106 mT was applied such that the splitting between the spin-conserving optical lines is larger to avoid cross-pumping of the electron spin. High-quality resonant Rabi oscillations without reduction of contrast can be observed for 9.5 ms [see Fig. 2(b)], which corresponds to an equivalent of 138 π pulses. This demonstrates that the superconducting waveguide can provide extended continuous rf driving without heating, which otherwise represents a challenge for many experiments [8,13,14,22]. For these long Rabi measurements, we determine a visibility to account for slow drifts of the emitter during the measurement time. Therefore, we use two Rabi measurements with different pulse lengths, where the second Rabi pulse duration is extended by a single π-pulse length, resulting in a 180° phase shift. The visibility is then calculated as $V = (S_0 - S_{180})/(S_0 + S_{180})$, where S indicates the

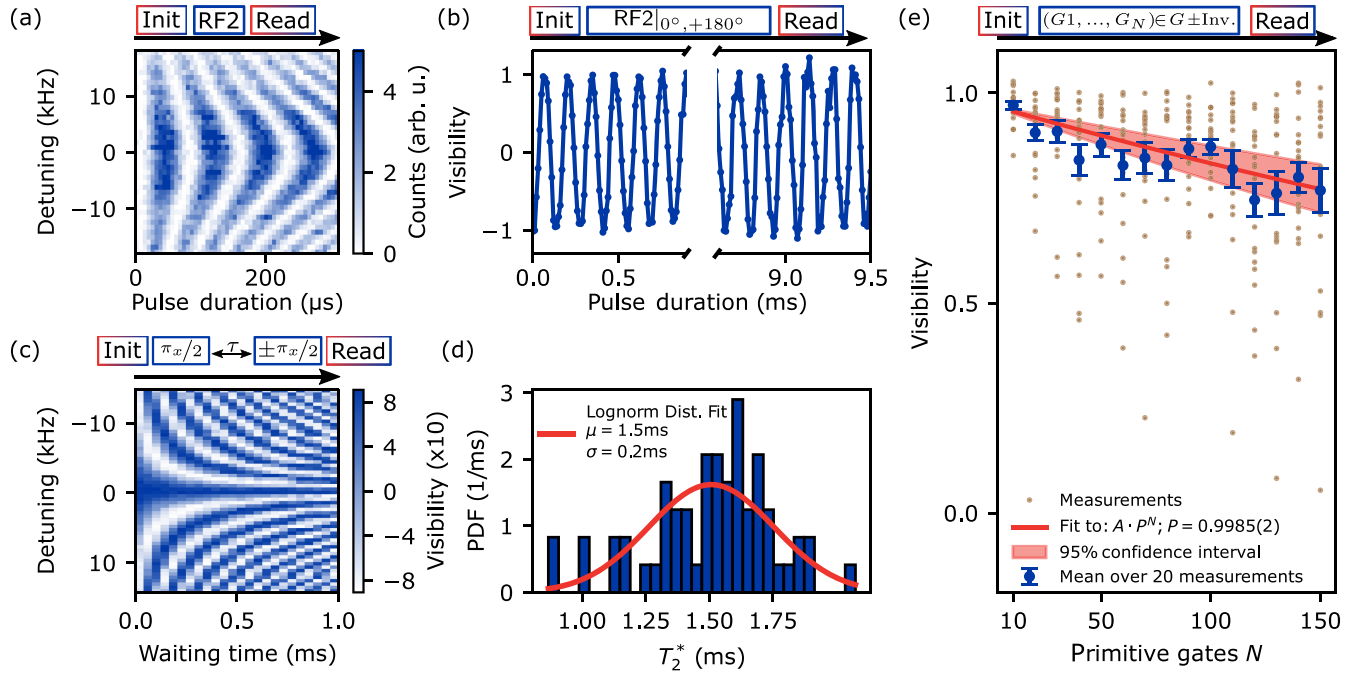

FIG. 2. (a) Chevron pattern of Rabi oscillations for various detunings. (b) Rabi oscillation over a pulse length of up to 9.5 ms. (c) Chevron pattern observed by detuned Ramsey measurements showing the stability of the qubit frequency. (d) Histogram of all coherence times for varying detunings leading to a mean coherence time of $\bar{T}_2^* = 1.5(1)$ ms. (e) Randomized benchmarking, where 20 realizations of random gates from the primitive gate set are performed. Each realization is repeated 500 times, and each blue point on the graph is the mean value of all different realizations. The error bars correspond to the standard error of the mean. The fidelity per primitive gate is $F_G = 1 - (1 - P)/2 = 99.92(1)\%$.

counted fluorescence of the readout pulse on each of the two sequences.

To measure the coherence and frequency stability of the nuclear-spin transition, a Ramsey sequence was performed for various detunings around 20.53 MHz; see Fig. 2(c). Again, a visibility measurement is implemented to give a direct measure of the nuclear-spin state population. Therefore, every measurement sequence is repeated with a 180° phase shift on the second $\pi/2$ pulse, and the visibility is calculated as above. The full Ramsey chevron measurement is performed over a total measurement time of four days and shows no large frequency jumps of the nuclear transition [see Figs. 2(c) and 12 in Appendix C 5]. Fitting each oscillation by a sine multiplied with an exponential decay $\exp[-(t/T_2^*)^2]$ gives the decoherence time T_2^*. A histogram of the coherence times for all detunings leads to a mean coherence time of $\bar{T}_2^* = 1.5(1)$ ms; see Fig. 2(d). Note that we can drive Rabi oscillations without any decay even for pulse durations much longer than the T_2^* time [see Fig. 2(b)]. This shows that the dephasing originates from slow spectral diffusion.

V. RANDOMIZED BENCHMARKING

To quantify the achievable fidelity for single-qubit gates, we perform randomized benchmarking. We use the set of primitive gates, consisting of the identity operation I, 90° rotations around the x and y axis of the qubit labeled as X and Y, respectively, and 180° rotations around the same axis, X^2 and Y^2. This forms the set $G = \{I, \pm X, \pm Y, \pm X^2, \pm Y^2\}$ [9,24]. The identity is defined as a waiting time of the same duration as the X^2 pulse to mimic a possible waiting time for a nuclear-spin memory readout or transfer. For each realization of a primitive gate sequence, a random selection out of G is taken. The inverse gate for the whole sequence is found and added to the sequence as a final additional gate [24]. To obtain a normalized visibility, the sequence is performed twice with two different π-shifted phases of the final inverse gate. Each visibility measurement uses 20 random realizations to ensure a statistical distribution of each number of gates used, each repeated 500 times to collect enough counting statistics. The mean value of these measurements is marked by blue dots in Fig. 2(e). This mean value can be fitted by the function $A \cdot P^N$, where A is a constant overall fidelity, combining initialization and readout fidelity, P is the fidelity per gate operation, and N is the number of gates [24]. The fidelity per primitive gate is then given by $F_G = 1 - (1 - P)/2 = 99.92(1)\%$. The factor $1/2$ accounts for the gate set being performed twice [24]. This primitive single-qubit gate fidelity can be expressed into the more commonly used single-qubit Clifford gate fidelity [24,25] of 99.85(2)%.

VI. DYNAMICAL DECOUPLING

To cancel the influence of slow fluctuations of the surrounding nuclear-spin bath, the coherence can be extended with a Hahn-echo sequence. As shown in Fig. 3 (gray data and fit), the corresponding decay of the visibility follows a stretched exponential decay corresponding to $A \cdot \exp[-(2\tau/T_2)^{\xi}]$, where A is the initial decoupling fidelity, T_2 the coherence time, and ξ the stretching factor of the exponential. We find an extended coherence time of $T_2 = 167(9)$ ms and $\xi = 1.7(2)$. Assuming an Ornstein-Uhlenbeck model for the bath noise [14,26], we obtain a bath coupling strength of 930(90) Hz from the coherence time T_2^*. This coupling strength of the bath is similar to the observed ODNR linewidth of the rf transition, as well as in the same order of magnitude as the detuning distribution in the Ramsey chevron pattern and the observed detuning in the 9.5-ms-long Rabi measurement (see Appendix C 1), indicating slow spectral diffusion of the nuclear-spin transition. In addition, we obtain a correlation time of the bath $\tau_c = 340(90)$ s, which is comparable to recent work on a single ^{13}C nuclear spin strongly coupled to a GeV center [14].

In order to estimate the possible extension of coherence, we perform dynamical decoupling with a CPMG sequence. In this sequence, the decoupling π pulses are 90° phase shifted with respect to the first $(\pi/2)$ pulse. For each number of pulses, we vary the delay time 2τ between the pulses and fit the decaying visibility. For a single decoupling pulse, we obtain a coherence time of $T_2(1) = 233(8)$ ms. Increasing the number of decoupling pulses prolongs the coherence time up to $T_2(128) = 1.35(3)$ s using 128 decoupling pulses. This is still not limited by the electron-spin lifetime (see Appendix C 2). We find that a stretched exponential decay $\propto \exp[-(2\tau/T_2)^{\xi}]$ with a stretching factor of $\xi = 2.0(1)$ describes the observed coherence decay best. The inset in Fig. 3 shows the scaling of the coherence time with the number of decoupling pulses, which follows a power law $T_2 \propto N^{\beta}$ with exponent $\beta = 0.37(1)$, which is lower than the expected 2/3 scaling for an Ornstein-Uhlenbeck model of the bath noise. We attribute this to the proximity of our defect to the diamond surface (in contrast to Ref. [14], where the GeV center is located inside a solid immersion lens), leading to additional noise baths on the diamond surface. As we observe a significant improvement between the coherence time T_2^* in the Ramsey decay and the echo coherence time, we conclude that the estimation of the bath coupling and bath correlation time above is still a good estimation for a slow fluctuating spin bath [26–28]. We note further that no visibility reduction occurs for increasing pulse number, pointing to the possibility to further extend coherence using more pulses.

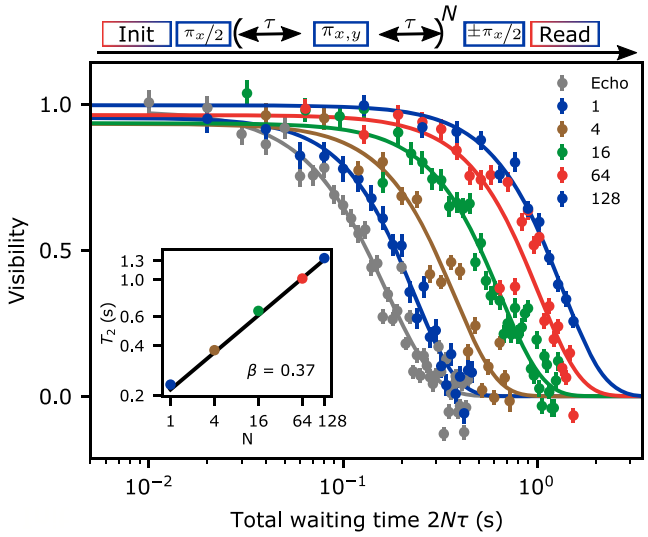

FIG. 3. Extended coherence using dynamical decoupling. A Hahn-echo sequence shows a coherence time of $T_2 = 167(9)$ ms (gray data and fit line). Colored data and fits show dynamical decoupling via a CPMG sequence fitted by a stretched exponential with stretching factor $\xi = 2$. The error bars correspond to the uncertainty of the visibility based on Poissonian statistics, giving the uncertainty as the square root of the mean counts measured for each waiting time and then propagated to an uncertainty on the visibility. The coherence time is increased from initially 232(7) ms to 1.35(3) s using $N = 128$ decoupling pulses. The inset shows the scaling of the coherence time T_2 with number of pulses N.

VII. CONCLUSION AND OUTLOOK

We have demonstrated high-fidelity control of a single ^{13}C nuclear spin utilizing readout via the electron spin of the SnV center. We harness a simple pumping scheme that provides high-fidelity initialization. Employing a superconducting CPW with smaller gap sizes than reported earlier [6] enables the demonstration of extended nuclear Rabi oscillations at low driving power with no signs of heating. We use dynamical decoupling to prolong the coherence up to 1.35(3) s, reaching a state-of-the-art level as desired for quantum network applications. The control fidelity is quantified by performing randomized benchmarking and achieves values that approach the requirements for quantum error correction [18].

Long-lived nuclear spins can serve as quantum memories in quantum network nodes, and a key aspect is how much the spin is affected by optical excitation of the electron to generate spin-photon entanglement. We measure the depolarization of the nuclear spin under optical excitation and find that the nuclear spin depolarizes after 3.7(9) electron-spin flips on average (see Appendix C 2). We also assess the decoherence of the nuclear spin under optical excitation due to the different hyperfine splittings in the ground and excited state. We find a comparably small difference of 2.6(6) MHz (see Appendix C 3), which can allow up to approximately 10^4 entanglement attempts before the nuclear memory decoheres. This emphasizes the potential of proximal nuclear spins as quantum node memories.

In addition, the studied spin is coupled to near-Fourier-limited optical transitions that show only marginal spectral diffusion. Such a combination of high control fidelity and long coherence time of a nuclear-spin qubit together with coherent and stable optical transitions fulfills key requirements for spin-photon interfaces and substantiates the potential of SnV centers for quantum network applications.

ACKNOWLEDGMENTS

We thank Michael Kieschnick and Jan Meijer for implanting the diamond sample. We thank Vadim Vorobyov, Katharina Senkalla, Fedor Jelezko, Matthias Müller, and Florian Ferlemann for insightful discussions. We thank Thomas Koch and Viktor Adam for helpful discussions and providing scripts for the randomized benchmarking measurements as well as Julia Heupel for technological support. This work was partly supported by the German Federal Ministry of Research, Technology and Space (Bundesministerium für Forschung, Technologie und Raumfahrt, BMFTR) within the projects QR.N (Contracts No. 16KIS2186, No. 16KIS2204, and No. 16KIS2180K), QR.X (Contracts No. 16KISQ004 and No. 16KISQ001K), SPINNING (Contract No. 13N16211), the Deutsche Forschungsgemeinschaft (DFG) through TRR 306-429529648 "QuCoLiMa," the Max Planck School of Photonics (MPSP), and the Karlsruhe School of Optics and Photonics (KSOP).

DATA AVAILABILITY

The data that support the findings of this article are openly available [29].

APPENDIX A: EXPERIMENTAL DETAILS

1. Sample fabrication and setup

The diamond sample used in this paper is cut in the ⟨110⟩ directions with a (100) surface with respect to the optical axis. The diamond is etched down along the (100) surface to a total thickness of 26 μm to relieve strain remaining from the manufacturing polishing and reducing the surface roughness [30]. The SnV centers are created by implantation of tin ^{116}Sn ions at an energy of 65 keV into the diamond and a subsequent annealing of 1200 °C for 4 h. For further details on the membrane fabrication, see Refs. [6,30]. Cleaning is performed by boiling with a 1∶1∶1 mixture of nitric, sulfuric, and perchloric acid (tri-acid cleaning) and subsequent piranha boiling. The diamond is glued with a thin layer of UV-curing adhesive (NOA63) onto an undoped silicon wafer to mitigate background fluorescence. The layer of UV curing glue was chosen to be much thinner compared to previous measurements in Ref. [6] to introduce less strain and achieve higher optical cyclicity [9]. The sample is mounted on a copper cold finger in a home-built dilution cryostat with a base temperature of 50 mK, surrounded by a 3D vector magnet. Optical access is given through an objective (Olympus MPlanN 100×/0.9 NA) and optical windows toward a confocal microscope setup as described in detail in our previous work [6].

Characterizing angular magnetic-field sweeps and ODMR were carried out on a total of six selected SnV centers within this sample (labeled SnV A to SnV F). SnVs A–C were used for the detailed analysis of the SnV center electron-spin Hamiltonian in Ref. [6], with SnV B used to demonstrate coherent control of the electron spin. ODMR on SnV D was performed by using a CPW made of gold [6]. SnV F is used throughout this work. All SnV centers investigated so far exhibited a visible coupling to nearby ^{13}C nuclear spins with varying coupling strengths, mostly in the range of 1–6 MHz. The SnV center in this work (SnV F) was the first in which coherent control of the ^{13}C nuclear spin was attempted and measured. Assuming the natural abundance of 1.1% ^{13}C nuclear spins, this corresponds to an expected probability of 6.6% for finding a nearest-neighbor ^{13}C nuclear spin on average.

2. Transition frequencies of the electron-nuclear coupled system

The electron-spin Hamiltonian can be found by fitting the differences in spin-conserving transitions as well as the ODMR frequencies to the eigenvalues of the Hamiltonian (see Ref. [6]). We find a low strain of 41.3(8) GHz in the ground state and a strain of 65.5(34) GHz in the excited state as shown in Fig. 4. Table I summarizes the fit parameters. Using this fit value allows for precise estimation of all electron transition frequencies for arbitrary orientations or magnitudes, reducing measurement overhead significantly.

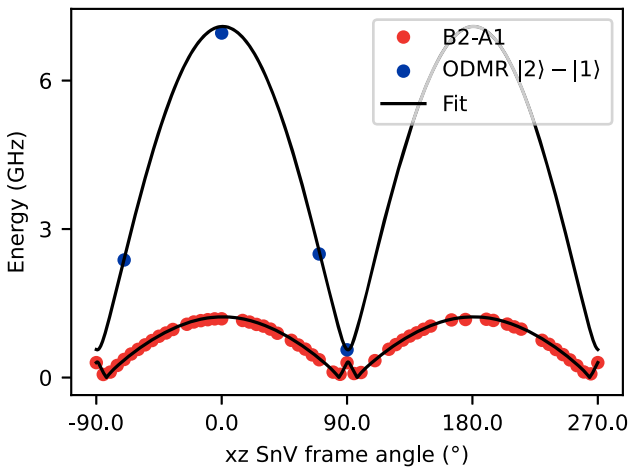

FIG. 4. Fit of the electronic energies of the SnV center to the observed optical-spin-conserving transitions A1 and B2 in the SnV frame (red points). The qubit transition frequencies (blue points) are measured in ODMR scans at 50 mK.

TABLE I. Fitted strain for the ground and excited states with the relevant Hamiltonian parameters taken from Ref. [6].

Parameter	Value	Source
λ^{g} (GHz)	822	[6]
Υ^{g} (GHz)	41.3(8)	Fitted
λ^{e} (GHz)	3000	[21,31]
Υ^{e} (GHz)	65.5(34)	Fitted
f_{12}^{g}	0.251	[6]
f_{32}^{g}	0.268	[6]
f_{12}^{e}	0.5	[6]
f_{32}^{e}	0.486	[6]
$B_{\parallel}$ (mT)	200	Fixed
$B_{\perp}$ (mT)	200	Fixed

The ODNR transitions RF1 and RF2 are shown in Fig. 5 for a magnetic field of 60 mT for qualitative purposes. The ODNR measurement is performed via a chirp over the resonance with −23 dBm rf power while continuously pumping the MW1 transition with −19 dBm and the spin-conserving optical transition B2 (A1) for RF1 (RF2), respectively. For RF1, a fit to two Lorentzian yields a FWHM of 1.5(2) kHz and a splitting $\Delta = 3.81(5)$ kHz, indicating coupling to a second ^{13}C nuclear spin. The transition RF2 yields a single Lorentzian. Therefore, all experiments are performed on the RF2 transition, where no coupling to a second nuclear spin is observed.

We expect that the two different electron-spin states $|\uparrow_e\rangle$ and $|\downarrow_e\rangle$ change the orientation of the electron spin's dipolar field and, thus, rotate the total magnetic field at the second nuclear spin, causing its quantization axis to change in such a way that nuclear-nuclear coupling appears only in the $|\downarrow_e\rangle$ configuration and is effectively absent in $|\uparrow_e\rangle$.

A fit yields a FWHM of 0.94(4) kHz in good agreement with the coherence time T_2^* shown in the main text.

3. Microwave power characterization

The microwave transmission setup inside the cryostat is described in Ref. [6]. The only difference in the interior setup is the superconducting coplanar waveguide made of niobium that is used for this work, which is a newly fabricated CPW with a constriction and narrow gaps at the end of the shorted circuit. The CPW has a conductor width of 30 μm at the shorted end and a gap width of 5 μm. A 3D model of the niobium CPW, created in Ansys HFSS, is depicted in Fig. 6(a). The narrow gaps confine the alternating magnetic field B_{ac} within, allowing fast qubit control at comparable low microwave input powers. In the following, we want to discuss the magnetic-field amplitude of the MW and rf fields at the location of the SnV center in detail.

For all measurement configurations, the noted power values correspond to the instantaneous power derived from the MW or rf amplitude and are determined using a spectrum analyzer (Keysight N9323C) in front of the input to the cryostat. This way, passive elements, like the MW and rf filters, the attenuators, the combiner, and the coaxial cables, have no influence. The input return loss (S11) of the microwave lines and the sample inside the cryostat is depicted in Fig. 7. A local return loss minimum is located at 3.7 GHz, which corresponds to the splitting of the electron-spin sublevels for a magnetic field of 106 mT parallel to the

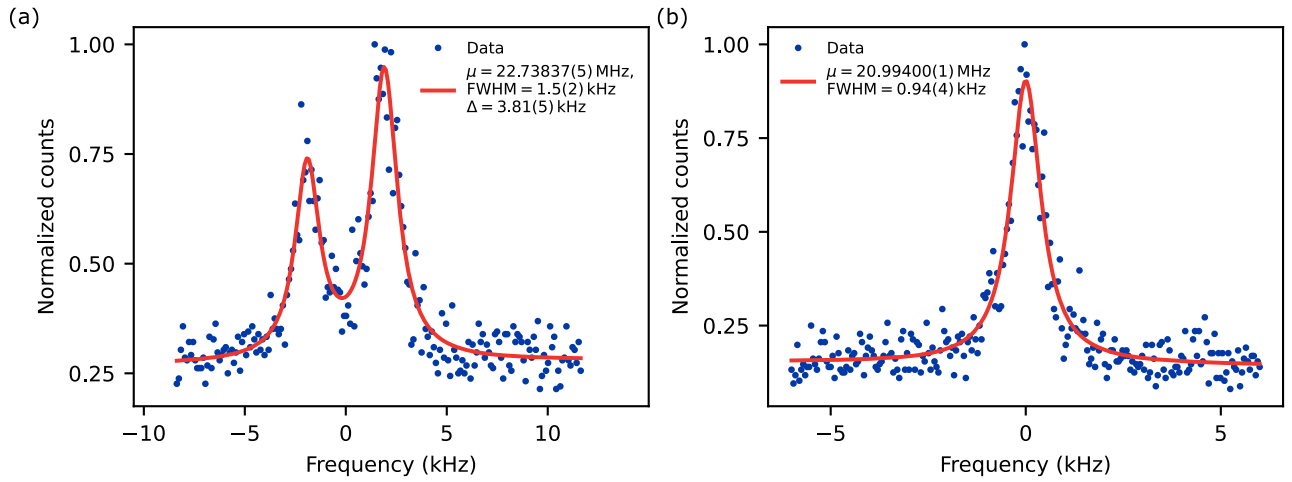

FIG. 5. (a) Transition frequency of the nuclear hyperfine transition RF1 at a dc magnetic field of 60 mT. Measured via a chirp over the resonance with −23 dBm while continuously pumping the MW1 transition with −19 dBm and the spin-conserving optical transition B2. A fit to two Lorentzian yields a FWHM of 1.5(2) kHz and a splitting $\Delta = 3.81(5)$ kHz. (b) Transition frequency RF2 measured in a similar way by pumping the A1 transition. A fit to a single Lorentzian yields a FWHM of 0.94(4) kHz, in good agreement with the coherence time T_2^* shown in the main text.

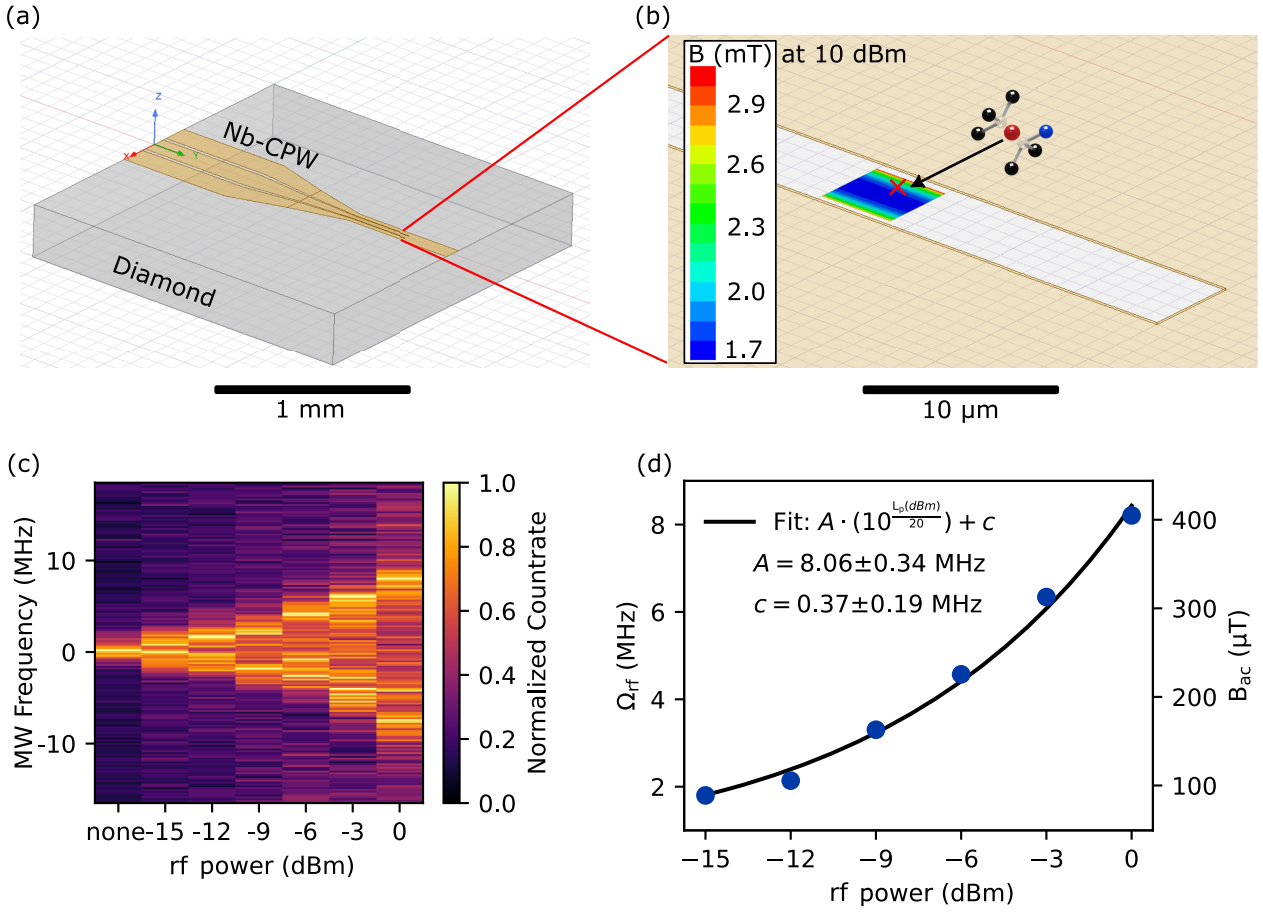

FIG. 6. (a) Model of the niobium CPW on a diamond substrate created in Ansys HFSS. (b) Simulation of the magnetic-field strength of the alternating microwave signal at 10 dBm input power into the structure. The simulation yields a field of 1.7 mT parallel to the z-lab axis. (c) Microwave spectrum of the electron transition versus the applied rf power under two-tone driving. (d) Amplitude of the frequency modulation as a function of the applied rf power.

SnV center axis. The loss up to the location of the SnV center is given by roughly half of the corresponding value.

For most of the coherent control measurements, we use a MW or rf input power of about 10 dBm. In the following, we characterize the magnetic field magnitude of the CPW for this value. In Fig. 6(b), the simulated magnetic field magnitude is depicted within the region of interest for a frequency of 20 MHz and 10 dBm excitation at the input of the structure. We note that the field intensity varies less than one percent at frequencies of 3 GHz according to frequency

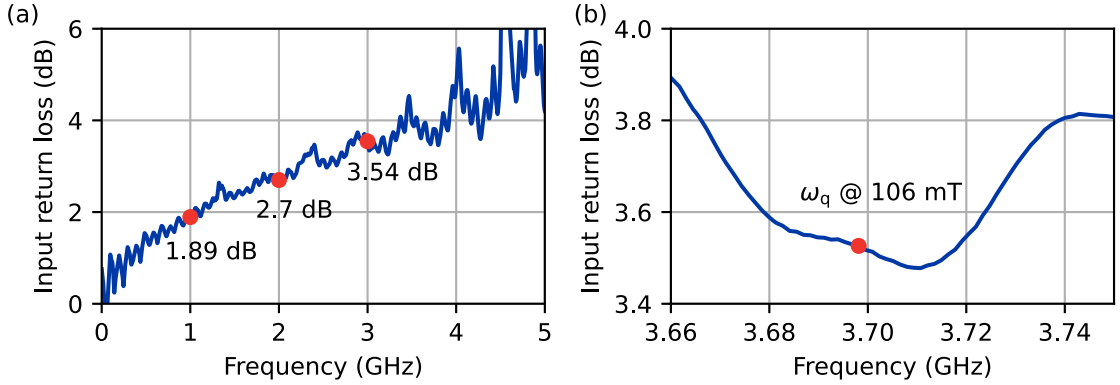

FIG. 7. (a) Input return loss of the microwave lines and the sample measured at the input port of the cryostat. (b) The transition of the electron-spin resonance is tuned to the local minimum of the input return loss by adjusting the magnetic dc field.

sweep simulations. At the center of the CPW gap, the simulation yields an B_{ac}-field magnitude of about 1.7 mT. The direction of the B_{ac} field at the surface of the gap is oriented perpendicular to the diamond surface, and, since the diamond is only negligibly misaligned to the z axis of the lab frame (approximately 0.1°), as spanned by the dc magnetic-field coils, the B_{ac} field shows purely in the z direction of the lab frame. For readers interested in the electromagnetic-field properties of CPWs, we refer to the work of R. Simons [32]. The SnV center is in close proximity to the surface (approximately 20 nm); therefore, we assume the same B_{ac}-field direction at its location.

To get a quantitative analysis of the B_{ac}-field magnitude, we conduct a two-tone spin resonance excitation of the SnV center. We excite the electronic spin transitions with a weak microwave signal and simultaneously apply a strong rf signal at a very low frequency of 10 kHz to modulate the qubit transition. In the rotating frame of the qubit, the slowly changing B_{rf} field can be described as an approximately constant component. Hence, while probing the spin transition, the energy splitting of the qubit ω_q takes a random value between $\omega_q - \Omega_{rf}$ and $\omega_q + \Omega_{rf}$ with an arcsine probability distribution. Here, Ω_{rf} refers to the maximum magnitude of the sinusoidal qubit transition modulation.

Following the approach in Refs. [33,34], adapted for our situation, the Hamiltonian in the rotating wave approximation (RWA) takes the form

$$H_{RWA} = \frac{1}{2}\Delta\omega\sigma_z + \frac{1}{2}\Omega_{MW}\sigma_x + \Omega_{rf}\cos(\omega_{rf}t)\sigma_z, \quad \text{(A1)}$$

where Ω_{MW} is the Rabi frequency and $\Delta\omega = \omega_q - \omega_{MW}$ is the detuning from the qubit resonance frequency. The Pauli matrix term with σ_x drives rotations about the x axis, while a z component is added by the magnitude of the detuning.

The third term is due to the B_{rf} field that modulates the qubit transition with the applied frequency $\omega_{rf} = 10$ kHz. Since we know the exact direction of the rf field and the orientation of the SnV center in the diamond, we can determine the amplitude of the frequency modulation by $\Omega_{rf} = \gamma_{SnV}(54.7°)B_{rf} = 20.27\ \text{MHz mT}^{-1}B_{rf}$. Here, we use the precise knowledge of the electron-spin Hamiltonian for this specific SnV center (see Fig. 4 for the corresponding fit) and the resulting gyromagnetic ratio for a magnetic field in the z direction in the lab frame. Figure 6(c) shows the resulting microwave spectrum versus the applied rf power. We fit each line of the spectrum to an arcsine probability distribution convolved with the Lorentzian line shape [33]. The splitting scales $\propto A(10^{[L_p(\text{dBm})/20]})$ as shown in Fig. 6(d). For an extrapolated rf power of 10 dBm, we extract a magnetic-field amplitude of $B_{ac} \approx 1.26$ mT, roughly 30% less compared to the simulation. The deviation can be explained relatively easily. The SMA connectors at the millikelvin plate to the flexible waveguide reflect about 0.5–0.7 dB, and an additional return loss of approximately 0.4 dB occurs at the bonding wires to the CPW on the diamond. These losses cannot be extracted from simple S11 measurements as depicted for the setup in Fig. 7 due to the low phase change of the reflected signals at kilohertz frequency. Please note that the magnetic-field component perpendicular to the SnV center's quantization axis that coherently drives the electron spin is given by $B_{ac}(35.3°) \approx 1.02$ mT. For a linearly polarized magnetic field, such as in our case, in the RWA only the corotating component with amplitude $B_{ac}/2$ drives the spin.

APPENDIX B: NUCLEAR-SPIN INITIALIZATION

1. Initialization fidelity

The nuclear initialization is fitted to an exponential decaying curve

$$A \cdot e^{-\gamma t} + C, \quad \text{(B1)}$$

using the PYTHON package lmfit [35], where each data point is weighted by $1/\sqrt{N+1}$, where N is the number of counts per data point, to attribute for Poisson noise statistics. The blue data points in Fig. 1(c) in the main text correspond to the initialization while driving the spin-conserving transition A1 and the microwave transition MW1 simultaneously. The red data points mark data taken with only the laser to correct for laser-induced background counts. To attribute for constant dark counts B, the brown data are taken with everything turned off. To calculate a fidelity, one has to subtract these background counts and calculate

$$F_{init} = 1 - \frac{C'}{A'}, \quad \text{(B2)}$$

where $C' = C - B$ and $A' = A - B$. Evaluating the data in Fig. 1(c) in the main text yields the parameters in Table II. To estimate the uncertainty of the initialization fidelity, we define the functions $g = A'^2 - C'A'$ and $h = A'^2$ and the fidelity as $F_{init} = g/h$. The uncertainty on g, h, and F_{init} is given by considering the partial derivatives, correlations ρ, and uncertainties σ. Using the fact that a higher background leads to higher counts, thus, the correlations $\rho_{AB} = 1$ and $\rho_{CB} = 1$ and the correlation coefficient of the fit $\rho_{AC} = 0.2235$. Using the correlation of $\rho_{gh} = 1$ and the

TABLE II. Parameters of the nuclear initialization fidelity estimation fit.

Parameter	Value	Standard deviation
Amplitude A	176	3
Decay γ	0.57 ms^{-1}	0.01 ms^{-1}
Background counts C	8.40	0.4
Dark counts B	8.08	0.01

values from fitted and obtained in Table II, we find an initialization fidelity of

$$F_{\text{init}} = 99.74(3)\% \tag{B3}$$

for the dark count corrected case and

$$F_{\text{init}} = 95.16(4)\% \tag{B4}$$

without dark count correction.

2. Electron and nuclear cyclicity

In order to determine the cyclicity of the nuclear-spin initialization, all relevant levels have to be considered. We start by a simplified three-level system as used in Refs. [17,36] to explain the electron-spin initialization dynamics. Following the derivation in Ref. [36], we have two spin levels $|\downarrow\rangle$ and $|\uparrow\rangle$ and an excited state $|A\rangle$, which is optically driven by the laser with an optical Rabi frequency Ω. The resulting Hamiltonian is

$$H = \Delta|A\rangle\langle A| + \frac{\Omega}{2}(|\downarrow\rangle\langle A| + |A\rangle\langle\downarrow|), \tag{B5}$$

where Δ is the detuning of the laser to the spin-conserving transition. Spontaneous emission into the spin ground states is implement by using the rates $\gamma_{A\downarrow}$ and $\gamma_{A\uparrow}$, respectively. Because of the low temperatures, spin flip rates directly between the two sublevels can be neglected. Following Ref. [17], we introduce a cyclicity $\Lambda_e = P_{A\downarrow}/P_{A\uparrow}$ given by the ratio of the probability to land in either spin state, and the rates can be expressed as $\gamma_{A\downarrow} = \gamma\Lambda_e/(1+\Lambda_e)$ and $\gamma_{A\uparrow} = \gamma/(1+\Lambda_e)$. Using the assumption that the spin-flipping rate $\gamma_{A\uparrow}$ is much smaller than the spin-conserving rate $\gamma_{A\downarrow}$, one can set the derivatives of the coherences $\dot{\rho}_{A\downarrow} = 0$ and $\dot{\rho}_{\downarrow A} = 0$ and end up with the quasistationary solutions of the master equation:

$$\dot{\rho}_{\downarrow\downarrow} = -W\rho_{\downarrow\downarrow} + (W+\gamma_{A\downarrow})\rho_{AA}, \tag{B6}$$

$$\dot{\rho}_{AA} = W\rho_{\downarrow\downarrow} - (W+\gamma)\rho_{AA}, \tag{B7}$$

where the rate W is given by $W = \Omega^2\gamma/(4\Delta^2+\gamma^2)$, dependent on the laser detuning Δ with respect to the spin-conserving transition [36]. The rate γ is given by 2π times the linewidth of the transition measured via PLE measurements. The resulting linewidth can be fitted by a Lorentzian curve (see Fig. 8) and results in $\gamma = 2\pi \cdot 36.6(1)$ MHz $=$ 230.0(6) MHz.

The optical Rabi frequency can be determined from a saturation measurement. For that, the resonant power p is increased and the count rate I recorded. Fitting to the model

$$I(p) = I_{\text{sat}} \cdot \frac{p/p_{\text{sat}}}{1+p/p_{\text{sat}}} + n_{\text{bgr}} \cdot p + C, \tag{B8}$$

where n_{bgr} stands for the background photon rate, one finds a saturation power of $p_{\text{sat}} = 29(3)$ nW. Using the relation between saturation power and Rabi frequency $p/p_{\text{sat}} = 2\Omega^2/\gamma^2$, we can convert the used optical power an optical Rabi frequency [37].

In order to measure the pure electron initialization, we initialize in the state $|\uparrow_e\downarrow_n\rangle$ by pumping for 10 ms with microwave MW1 at -16 dBm while continuously pumping the A1 transition. Afterward, a 304 ns π pulse of microwave MW2 at 17 dBm flips the electron-spin state

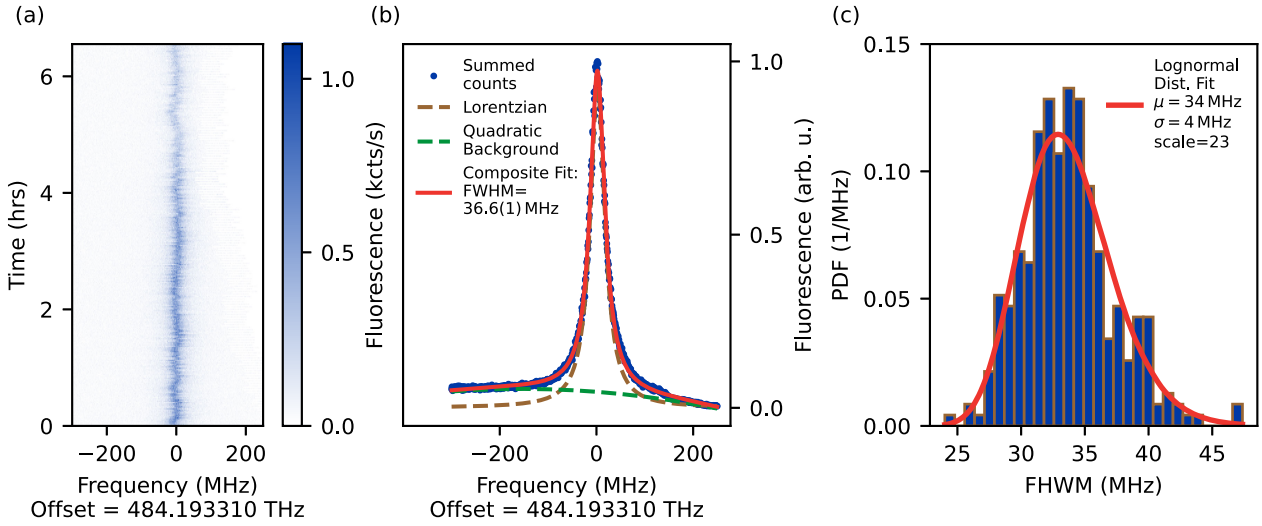

FIG. 8. (a) Photoluminescence excitation scan of the optical line A1 with a power of $p_{\text{PLE}} = 0.6$ nW $\approx p_{\text{sat}}/50$. The line remains stable over the course of over six-hour-long measurement. (b) Lorentzian fit to the sum of all individual scans in (a). This leads to a close to Fourier-limited line of 36.6(1) MHz. (c) Individual line fits for each scan result in a linewidth of 34(4) MHz in good agreement with the summed PLE scans showing negligible spectral diffusion.

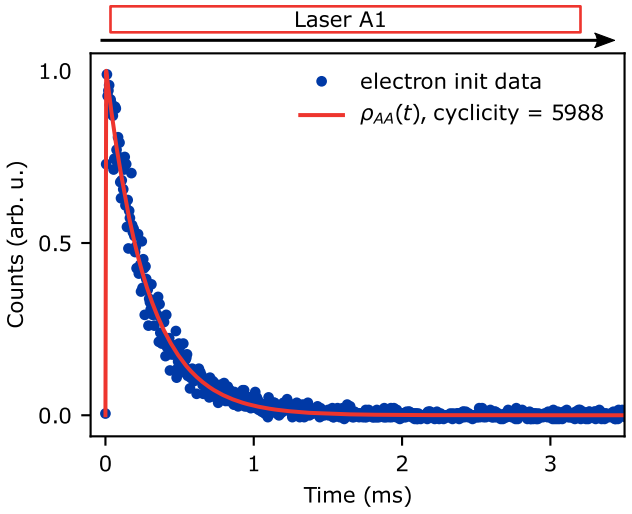

FIG. 9. Electron initialization curve measured by pumping the A1 transition. A fit to the rate equation (B7) leads to a cyclicity of $\Lambda_e = 5988$.

to $|\downarrow_e\downarrow_n\rangle$, and the initialization is measured by only driving the optical A1 transition with 7 nW power. The result is shown in Fig. 9. Assuming a detuning of $\Delta = \omega_{\mathrm{RF1}} = 22.74$ MHz, by setting the A1 transition in the center between the two hyperfine transitions, only the cyclicity is left as a free parameter. Fitting the model to the decaying fluorescence in Fig. 9 results in a cyclicity $\Lambda_e = 5988$. We note that, although the exact detuning Δ is unknown, a change from $\Delta = 0$ MHz to $\Delta = 2\omega_{\mathrm{RF1}}$ changes the estimated cyclicity only from 6177 to 5485, approving the robustness of the electron cyclicity estimation.

In order to estimate the cyclicity of the nuclear-spin-conserving transition, one has to consider all nuclear-spin states, leading to a total of six relevant levels. By expanding to the nuclear sublevels, we find the populations for ground g_i and excited state e_i:

$$\dot{g}_i = \sum_{j=0}^{1}(\gamma b_{ji} + R_{ji})e_j - R_{ji}g_i + W_{\mathrm{MW}}(\xi_{30}\delta_{i0} + \xi_{03}\delta_{i3}), \tag{B9}$$

$$\dot{e}_i = \sum_{i=0}^{3} R_{ji}\cdot g_i - (W+\gamma)\cdot e_j, \tag{B10}$$

where the states g_i are $\{|\downarrow_e\uparrow_n\rangle, |\downarrow_e\downarrow_n\rangle, |\uparrow_e\downarrow_n\rangle, |\uparrow_e\uparrow_n\rangle\}$ of the ground state manifold and $e_i = \{|\downarrow_e\uparrow_n\rangle, |\downarrow_e\downarrow_n\rangle\}$ of the excited state in ascending order and $\xi_{ij} = (g_i - g_j)$ the difference between the ground state populations. The rate W_{MW} describes the incoherent microwave pumping with MW1 during the initialization process with δ_{ij} as the Kronecker delta, therefore connecting the ground states g_0 and g_3. The matrix b_{ji} gives the probabilities P to flip/conserve the nuclear and/or electron spin, as indicated by the indices, and is defined as

$$b = \begin{pmatrix} P_{\mathrm{ec}}\cdot P_{\mathrm{nc}} & P_{\mathrm{ec}}\cdot P_{\mathrm{nf}} & P_{\mathrm{ef}}\cdot P_{\mathrm{nf}} & P_{\mathrm{ef}}\cdot P_{\mathrm{nc}} \\ P_{\mathrm{ec}}\cdot P_{\mathrm{nf}} & P_{\mathrm{ec}}\cdot P_{\mathrm{nc}} & P_{\mathrm{ef}}\cdot P_{\mathrm{nc}} & P_{\mathrm{ef}}\cdot P_{\mathrm{nf}} \end{pmatrix}, \tag{B11}$$

with the probabilities

$$\begin{aligned} P_{\mathrm{ec}} &= \Lambda_e/(1+\Lambda_e), \\ P_{\mathrm{ef}} &= 1/(1+\Lambda_e), \\ P_{\mathrm{nc}} &= \Lambda_n/(1+\Lambda_n), \\ P_{\mathrm{nf}} &= 1/(1+\Lambda_n). \end{aligned}$$

We introduced here the quantity Λ_n, which quantifies after how many electron-spin flips the nuclear spin becomes depolarized. Since this quantity is defined in an analogous manner as the electron cyclicity, we call it the nuclear cyclicity in the following sections.

The pump rates R are given by the matrix

$$R = \begin{pmatrix} W & 0 & 0 & 0 \\ 0 & W & 0 & 0 \end{pmatrix}, \tag{B12}$$

assuming only nuclear- and electron-spin-conserving optical pumping of the transitions. For these initialization measurements, very low MW powers are used. The resulting Rabi frequency can be calculated by using the electron-spin Rabi measurement in Fig. 16(a). For a driving power of 16 dBm, we observe a Rabi frequency of $\Omega_{\mathrm{MW1}} = 1.59(1)$ MHz. The resulting attenuated Rabi frequency is given by $\Omega_{\mathrm{att}} = \Omega_{\mathrm{MW1}}10^{(\mathrm{att}/20)}$, where a typical attenuation is about -35 dB. While the rate model qualitative reproduces the temporal behavior of the initialization for different starting ground states, the incoherent spin pump rate needs to be defined in order to estimate the nuclear cyclicity. In analogy to the incoherent optical pumping above, we define the incoherent rate as $W_{\mathrm{MW}} = \Omega_{\mathrm{att}}^2\gamma_{\mathrm{e,sp}}/(4\Delta_{\mathrm{MW}}^2 + \gamma_{\mathrm{e,sp}}^2)$ with the detuning of the microwave Δ_{MW} and the linewidth of the spin transition $\gamma_{\mathrm{e,sp}}$. The linewidth of the spin transition without any applied optical fields can be approximated by the coherence time $1/T_2^*$, which yields a linewidth of $\gamma_{\mathrm{e,sp}} = 1.4(4)$ MHz [see Fig. 16(c)]. However, measuring the resulting dark spin pump rate is not possible as $\Omega_{\mathrm{att}} \ll 1/T_2^*$, yielding only a contribution to the signal when the electron spin is resonant to the microwave tone, resulting in too small observed rates in the few 10–100 Hz ranges. Because of the optical pumping during the initialization process, the spin resonance is broadened to the optical Rabi frequency. However, measuring the resulting incoherent spin pump rate under these conditions is not directly accessible.

If we use the estimation found in Appendix C 2 and use a nuclear cyclicity of $\Lambda_n = 3.7(9)$, we find an effective

linewidth $\gamma_{e,sp} \approx 0.49$ MHz, in reasonable agreement with $1/T_2^*$.

APPENDIX C: COHERENT CONTROL

1. Nuclear Rabi frequency enhancement

Placing a nuclear spin in close proximity to an electron spin enhances the nuclear Rabi frequency by mixing of electronic character into the nuclear-spin levels [38,39]. To estimate this enhancement of the nuclear Rabi frequency, we measure it as function of the external applied dc magnetic field from −300 to 300 mT parallel to the SnV axis. For each dc magnetic field, due to the frequency-dependent losses in the microwave setup (e.g., the narrow-band rf filter), the rf field B_{ac} is calculated using the calibration from the previous section. A comparison to the gyromagnetic ratio of the ^{13}C nuclear spin gives an estimation of the enhancement due to the nearby electron spin [38,39]. The resulting Rabi frequency is given by

$$\Omega_{nuc} = \gamma_{^{13}C}/2 \cdot \xi \cdot B_{ac}, \tag{C1}$$

with the gyromagnetic ratio $\gamma_{^{13}C} = 10.7\ \mathrm{kHz\,mT^{-1}}$. The factor $1/2$ attributes for the linear polarized microwave field, where only the corotating circular polarization is driving the nuclear spin.

The nuclear Rabi frequency depends on the relative angles of the magnetic moment of the ^{13}C nuclear spin and the B_{ac} field orientation. For small dc fields, the dipole-dipole coupling term dominates and sets the precession axis of the ^{13}C nuclear spin. As the dc field increases, the ^{13}C precession axis tilts toward the direction of the external dc field, which coincides in this experiment with the quantization axis of the SnV center. Depending on the position of the

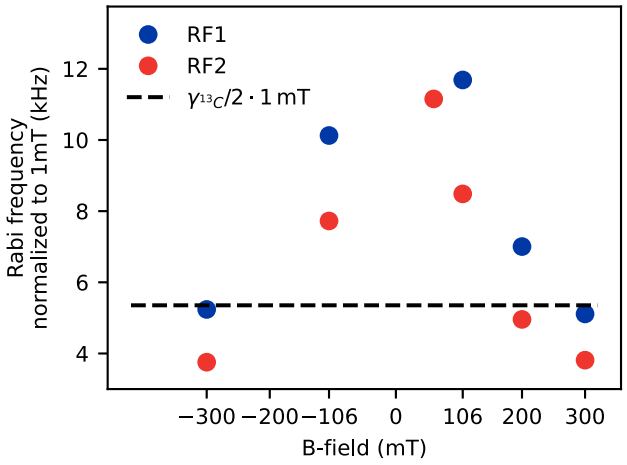

FIG. 10. Nuclear Rabi frequency as a function of the dc magnetic field aligned parallel to the SnV center axis. With increasing amplitude of the dc magnetic field, the Rabi frequency decreases. The free Rabi frequency for a linear polarized microwave field perpendicular to ^{13}C nuclear spin is denoted by a black dashed line.

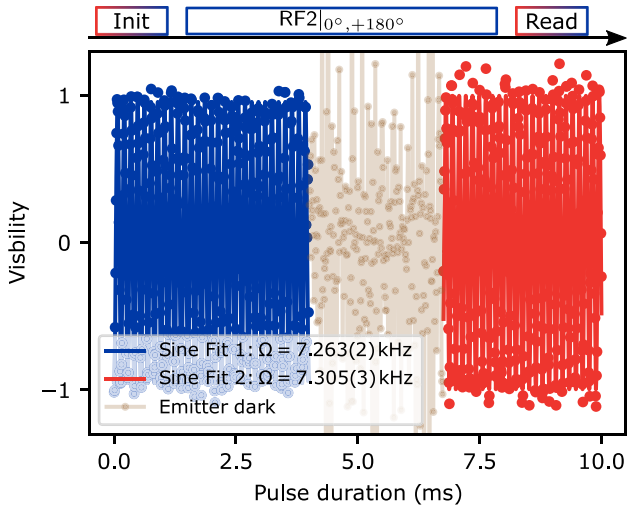

FIG. 11. Long Rabi oscillation with intermediate repump. The Rabi oscillation before the repump of 7.263(1) kHz differs only slightly from the oscillation after of 7.305(3) kHz. This would correspond to a detuning of the line of 826(30) Hz.

^{13}C nuclear spin relative to the SnV center, the tilt can coincide with the orientation of the B_{ac} field, thus creating a local minimum of the Rabi frequency as the field increases. Only at very strong dc fields should the Rabi frequency approach that of the free ^{13}C nuclear spin.

Thus, the measurements of the Rabi frequency in Fig. 10 are normalized to a field $B_{ac}^{SnV,\perp} = 1$ mT perpendicular to the SnV axis using the calibration above in Appendix A 3, as this is the expected setting giving the driving strength for a free ^{13}C nuclear spin under optimal conditions. We observe a maximum enhancement of $\xi(60\ \mathrm{mT}) = 2.06(1)$, which yields a nuclear Rabi frequency roughly twofold faster than the expected free Rabi frequency.

To quantify the heating effect and loss of coherence due to steady driving, we measure Rabi oscillations up to 10 ms pulse length with a power of 10 dBm at a field of 106 mT, where the enhancement is $\xi(106\ \mathrm{mT}) = 1.6(2)$. To compensate for emitter drifts or laser fluctuations during this long measurement, we determine a visibility using two subsequent Rabi measurements, where the second Rabi pulse duration is extended by a single π-pulse length of 69.25 μs, resulting in a 180° phase shift. The visibility is then calculated as $V = (S_0 - S_{180})/(S_0 + S_{180})$, where S indicates the counted fluorescence. The result is shown in Fig. 11. The emitter lost its charge state during the measurement sequence but was recovered by a 532 nm laser pulse. The change in the fitted Rabi frequency from 7.263(2) to 7.305(3) kHz can be attributed to detuning of $\Delta = 826(30)$ Hz, which is on par with the spectral diffusion discussed in Sec. VI in the main text. This shows that we can drive the nuclear spin for extended times without any signs of heating. The increase of noise in the visibility can be attributed to a slow spatial drift of emitter and

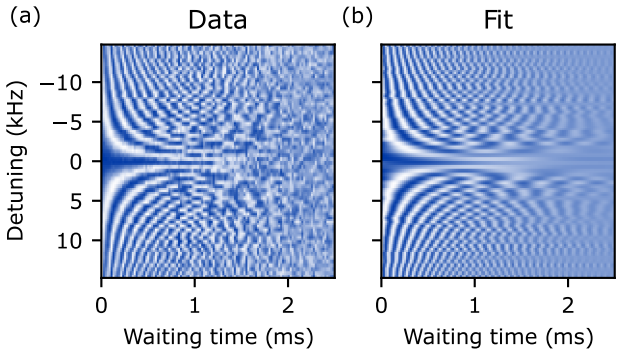

FIG. 12. (a) Ramsey measurements of RF2 for varying detunings up to a waiting time of 2.5 ms. (b) Fitting each row with $\exp[-(t/T_2^*)^2]$ gives the coherence time given in the main text.

corresponding reduction of fluorescence during the experiment of about 18 h.

In extension to the Ramsey chevron pattern depicted in Fig. 2(c), we show here the full Ramsey measurement used for calculating the coherence times given in Fig. 2(d). Fitting each row to the expected Gaussian decay $\exp[-(t/T_2^*)^2]$ generates the fits in Fig. 12(b), where we can see small deviations of the detuning over the course of the measurement. We note that the total measurement duration was approximately 100 h.

2. Nuclear depolarization under optical excitation

An important question for the realization of quantum network nodes is how much a proximal nuclear spin is affected by optical excitation of the electron spin. As a first step, in order to quantify the nuclear-spin depolarization, we measure the electron-spin lifetime. We initialize the system in the substate $|\uparrow_e\downarrow_n\rangle$ by pumping A1 and MW1, followed by a waiting time t_{wait} and subsequent readout. For the bright (dark) readout, we apply (do not apply) an RF2 π pulse before the readout pulse, and we define the contrast as the bright readout counts divided by the sum of the bright and dark counts. The resulting contrast as a function of t_{wait} is shown in Fig. 13(a) as the blue curve, labeled C_1. We observe no decrease in this contrast and, therefore, conclude that there is no measurable effect associated with the electron-spin lifetime T_1 for waiting times up to 30 s.

To investigate the depolarization rate R_{dp}, we repeat the same pump-probe measurement but keep the laser resonant with A1 continuously on, during the waiting time t_{wait}. After initialization, the electron occupies the spin state whose resonant optical transition is B2, while the laser is tuned to A1. Therefore, excitations can occur only off-resonantly via the Lorentzian tail of the A1 line overlapping with B2, leading to occasional excitation into the optically excited state. These excitations can still lead to an electron-spin flip (see Appendix B 2) and, thus, to a flip of the nuclear spin [14]. With increasing waiting time under

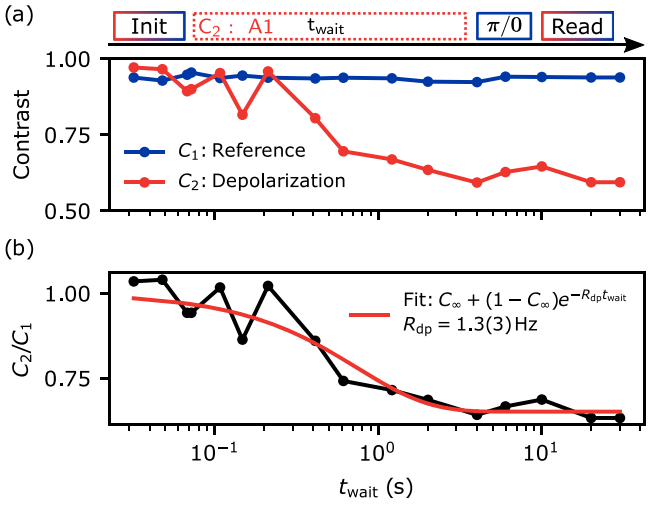

FIG. 13. Measurement of the electron-spin population and nuclear-spin depolarization. (a) Electron-spin population after initialization followed by a varying waiting time t_{wait}, an RF2 π pulse, and subsequent readout. The contrast C_1 shows no decrease on these timescales, indicating an electron-spin lifetime $T_1 \gg 30$ s. When the laser is applied during the waiting time, the contrast decreases (C_2) due to nuclear-spin depolarization. Both contrasts are corrected using a reference sequence in which the RF2 π pulse is omitted after the waiting time. (b) Ratio C_2/C_1, showing the normalized decay due to nuclear-spin depolarization. An exponential fit yields a depolarization rate of 1.3(3) Hz.

the additional A1 illumination, we observe a decrease in the contrast, labeled C_2 in Fig. 13(a) (red curve). Fitting the ratio of C_2 and C_1 to an exponential decay of the form

$$C_2/C_1 = C_\infty + (1 - C_\infty)e^{-R_{\mathrm{dp}}t_{\mathrm{wait}}} \tag{C2}$$

yields a depolarization rate of $R_{\mathrm{dp}} = 1.3(3)$ Hz [see Fig. 13(b)].

To determine how many optically induced electron-spin flips correspond to the observed depolarization rate, we compare the background-corrected counts obtained under off-resonant excitation and measure the difference in count rates between driving on A1 and illuminating with the laser detuned by −9.6 GHz, with a total measurement time of 30 min for each setting. At a resonant laser power of 9.2 nW, we observe a count rate of $S_{\mathrm{A1}} = 30.419(3)$ Hz on A1 and $S_{\mathrm{det}} = 23.689(3)$ Hz when detuned and, thus, a difference of $S_{\mathrm{A1}} - S_{\mathrm{det}} = 6.730(4)$ Hz counts. To relate this to a electron-spin-flipping rate, we measure electron-spin initialization under the same experimental conditions, as described in Appendix B 2. We find an average background-corrected number of photons per electron initialization of $S_{\mathrm{init}} = 1.37(1)$, yielding an electron-spin-flip rate of

$$R_{\mathrm{flip}}(9.2\ \mathrm{nW}) = \frac{S_{\mathrm{A1}} - S_{\mathrm{det}}}{S_{\mathrm{init}}} = 4.9(4)\ \mathrm{Hz}. \tag{C3}$$

Comparing this to the depolarization rate allows us to estimate a nuclear cyclicity of

$$\Lambda_n = \frac{R_{\mathrm{flip}}}{R_{\mathrm{dp}}} = 3.7(9). \tag{C4}$$

One alternative approach to estimate the nuclear cyclicity is to perform dc magnetic-field angle-dependent measurements to map out the full hyperfine tensor and then infer the cyclicity from the change in the nuclear-spin quantization axis between the ground and excited states arising from the different dipole-dipole coupling [40].

3. Nuclear decoherence under optical excitation

Another important question is the decoherence of the nuclear spin under optical excitation due to the different hyperfine coupling in the electron ground and excited states [8,12,15]. To estimate the dephasing of the nuclear spin under optical excitation, we follow the approach of Ref. [8] and perform Hahn-echo-like measurements on the nuclear spin. First, the nuclear spin is initialized into $|\uparrow_e\downarrow_n\rangle$ by applying A1 and MW1. After applying an RF2 $(\pi/2)$ pulse to create a nuclear-spin superposition, we apply a laser pulse on A1 with variable duration t within a fixed nuclear-spin evolution time of, e.g., $\tau = 20$ ms. The nuclear spin is then refocused with a π pulse, a second waiting interval equal to the first, and projected with a final $(\pi/2)$ pulse, followed by readout. This sequence corresponds to the asymmetric configuration shown in Fig. 14(a). To normalize the signal, we repeat the sequence with a 180°-shifted final $(\pi/2)$ pulse. The resulting visibility oscillates due to a coherent phase accumulation obtained during the finite time spent in the excited state, which has a different Larmor precession than the ground state [8]. In addition, the oscillations are exponentially damped, because the time spent in the excited state is probabilistically distributed [12]. Applying a second laser pulse of equal length in the second waiting-time window [the symmetric case in Fig. 14(a)] cancels the coherent oscillation and leaves only the decoherence [8].

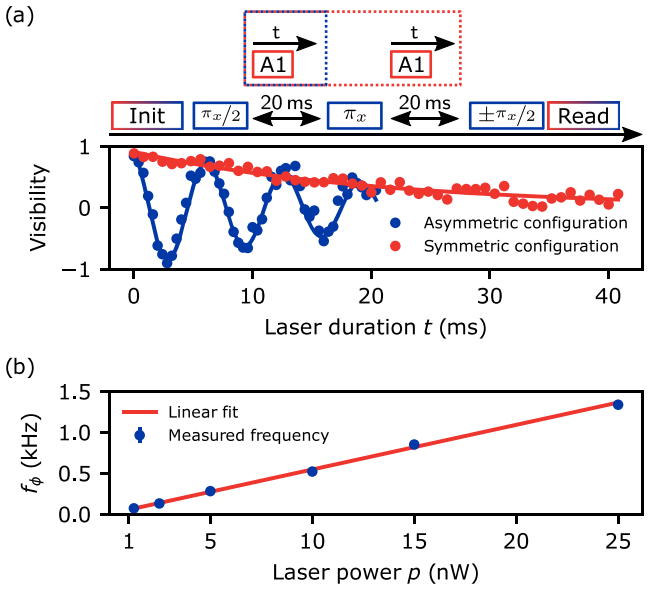

FIG. 14. Hahn-echo measurements on the nuclear spin with additional optical excitation during the waiting time between the echo control pulses. (a) Exemplary plot of decoherence in the excited state for asymmetric (blue data points) and symmetric configuration of optical pulses. (b) Power dependence of the oscillation frequency obtain via the asymmetric measurements. The error bars correspond to the standard error of the fitted frequency.

The phase accumulation is defined by the difference in the hyperfine splitting between ground and excited states and by the time spent in the excited state t_{exc}, as given in Ref. [12]:

$$\phi = (\omega_{\mathrm{HF}}^{\mathrm{exc}} - \omega_{\mathrm{HF}}^{\mathrm{gnd}}) \cdot t_{\mathrm{exc}}. \tag{C5}$$

Because an electron-spin flip destroys the accumulated nuclear phase, the measured phase evolution is sensitive only to the off-resonant excitations that occur without inducing a spin flip. Driving A1 while the electron occupies the B2 manifold, therefore, corresponds to a low effective saturation parameter $s_{\mathrm{eff}} = p_{\mathrm{eff}}/p_{\mathrm{sat}} \ll 1$, and we expect the time spent in the excited state to scale linearly with the applied laser power. We model this using the expression from Ref. [15]:

$$\frac{t_{\mathrm{exc}}}{t} = \frac{s_{\mathrm{eff}}}{2s_{\mathrm{eff}} + 1} \approx s_{\mathrm{eff}} = \frac{p_{\mathrm{eff}}}{p_{\mathrm{sat}}}, \tag{C6}$$

where (t_{exc}/t) gives the fraction of the time spent in the excited state [15]. Because of the detuning between A1 and B2 by $\Delta_{\mathrm{opt}} = 647$ MHz, the effective excited state population under driving B2 is reduced by the Lorentzian factor:

$$\frac{p_{\mathrm{eff}}}{p_{\mathrm{sat}}} = \frac{p}{p_{\mathrm{sat}}} \cdot \frac{1}{1 + \frac{4\Delta_{\mathrm{opt}}^2}{\Gamma^2}}. \tag{C7}$$

Here, Γ is the FWHM linewidth of the emitter. The detuning Δ_{opt} is set by the difference in orbital quenching factors between the ground and excited states, together with the magnetic-field component along the SnV center axis [6].

This means the phase-accumulation frequency is given by

$$f_\phi = \frac{\phi}{t} = \Delta_{\mathrm{HF}} \cdot \frac{t_{\mathrm{exc}}}{t} = \Delta_{\mathrm{HF}} \cdot \frac{p}{p_{\mathrm{sat}}} \cdot \frac{1}{1 + \frac{4\Delta_{\mathrm{opt}}^2}{\Gamma^2}}, \tag{C8}$$

which yields a linear dependence of the phase accumulation frequency on the applied laser power. As shown in

Fig. 14(b), we indeed observe a linear trend. Fitting $f_\phi = a \cdot p$ yields a slope of $a = 54.5(9)$ Hz nW^{-1}. From this, we estimate the difference in hyperfine splittings as

$$\Delta_{\mathrm{HF}} = a \cdot p_{\mathrm{sat}} \cdot \left(1 + \frac{4\Delta_{\mathrm{opt}}^2}{\Gamma^2}\right). \tag{C9}$$

We estimate the saturation power from an electron initialization measurement. Using the known cyclicity under this field configuration of $\Lambda_e = 5988$, we fit the initialization curve and obtain $p_{\mathrm{sat}} = 32(2)$ nW. With the measured $\Gamma = 34(4)$ MHz, this yields a difference in the hyperfine splitting of $\Delta_{\mathrm{HF}} = 2.6(6)$ MHz.

To validate this value, we perform count-rate measurements analogous to Appendix C 2 at a fixed excitation power of 10 nW, as an independent estimate of the time spent in the excited state. We infer the excitation rate from the photon rate detected under continuous (off-resonant) driving on A1. Using the measured photon rate and the number of photons per electron initialization defined above, we extract the electron-spin-flip rate. For this cooldown, we obtain $R_{\mathrm{flip}}(10\ \mathrm{nW}) = 8.1(1)$ Hz. We then convert this into an excitation rate:

$$R_{\mathrm{exc}}(10\ \mathrm{nW}) = \frac{1}{2}\Lambda_e R_{\mathrm{flip}}(10\ \mathrm{nW}) = 24.3(3)\ \mathrm{kHz}. \tag{C10}$$

The factor of $1/2$ accounts for the fact that under continuous A1 driving we detect, on average, twice as many photons per flip event, as after a spin flip the system becomes resonant with A1 and typically flips back rapidly, producing a second photon burst. In contrast, in the (asymmetric-)echo measurement, A1 is applied only for a short time and at low effective saturation, such that electron-spin flips during the pulse are negligible. The observed oscillation, therefore, reflects phase accumulation from off-resonant excitations without this rapid flip-back process. Measuring a single asymmetric echo configuration at this excitation power yields an oscillation frequency of 253(3) Hz. Together with the mean excited lifetime $\tau_{\mathrm{SnV}} = 1/\Gamma = 4.7(6)$ ns, this gives a difference in hyperfine splitting of

$$\Delta_{\mathrm{HF}} = \frac{f_\phi}{R_{\mathrm{exc}} \cdot \tau_{\mathrm{SnV}}} = 2.3(3)\ \mathrm{MHz}, \tag{C11}$$

in good agreement with the previously obtained result.

4. Outlook for use as network node

Knowing the difference in hyperfine splitting between ground and excited states allows us to estimate the reduction in nuclear-spin memory fidelity in network protocols that use optical π pulses. Using the model derived in Ref. [12], we can calculate how many optical π pulses n_{th} are required to fully decohere the nuclear spin. This is given by

$$n_{\mathrm{th}} = -2 \cdot \frac{\log(x)}{\log(1 + \Delta_{\mathrm{HF}}^2 \cdot \tau_{\mathrm{SnV}}^2)}, \tag{C12}$$

where x is the amount of excess fidelity remaining over the fully mixed state. The memory fidelity is then given by the relation $F_{\mathrm{mem}} = \frac{1}{2}(x + 1)$.

We find that a total number of optical π pulses of $n_{\mathrm{th}} \approx 10^4$ lead to a remaining excess fidelity of $x = 1/e$ or an equivalent memory fidelity of $F_{\mathrm{mem}} = 68\%$ for our given parameters. The total number of excitations needed scales inversely with the collection efficiency η of the setup [12]. We, therefore, consider the memory fidelity as a function of the number of successfully collected photons, which corresponds to the product $\eta \cdot n_\pi$, shown in Fig. 15. We estimate the collection efficiency by the ratio of the electron cyclicity $\Lambda_e = 5988$, which corresponds to the mean number of scattered photons during an initialization process and the number of photons collected per initialization [41] and find $\eta = 0.0208(3)\%$. While this value is low, it is expected, since our SnV center is located close to the surface in bulk diamond. For comparison with recent work using photonic structures in diamond, specifically solid immersion lenses [41] and photonic crystal cavities [42], we plot the fidelity for the same hyperfine splitting difference but using the collection efficiencies reported in those references. The results, shown in Fig. 15, yield substantially higher fidelity for the same number of collected

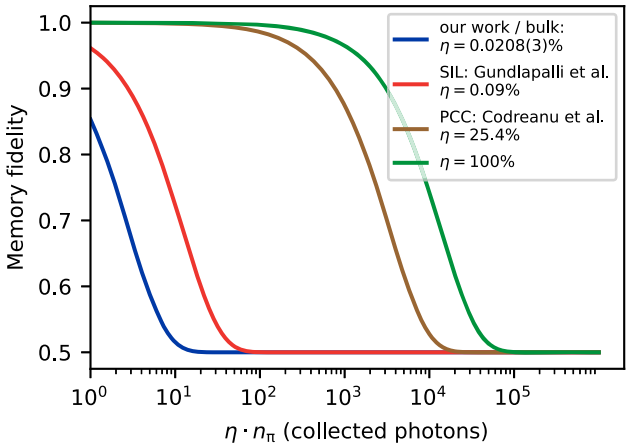

FIG. 15. Memory fidelity as a function of collected photons assuming n_π optical π pulses [12]. Different collection efficiencies result in different decays but showing effectively the same decoherence as a function of the number of optical π pulses, which is depicted as the green curve. A total number of approximately 5×10^4 of optical π pulses lead to a full decoherence of the nuclear spin.

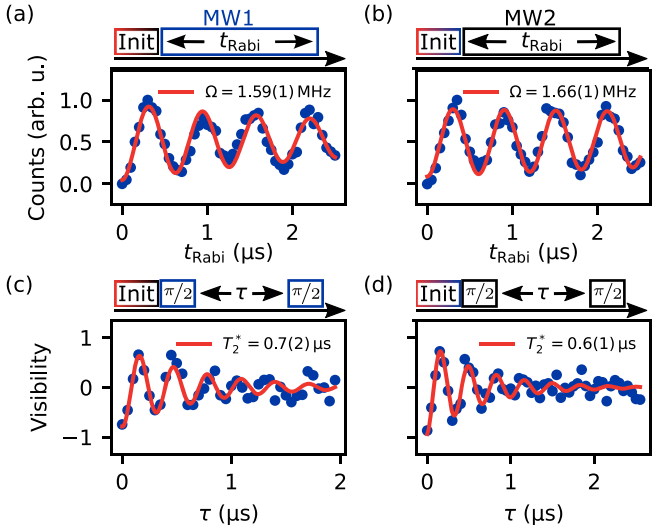

FIG. 16. Electron-spin control. (a) Single oscillation with a Rabi frequency of $\Omega = 1.59(1)$ MHz at 16 dBm power for transition frequency MW1. (b) Single oscillation with a Rabi frequency of $\Omega = 1.66(1)$ MHz at 14 dBm MW power for transition frequency MW2. (c) Ramsey decay of MW1 for a detuning of 3.22(5) MHz yielding a coherence time $T^*_{2(e)} = 0.7(2)$ μs. (d) Ramsey decay of MW2 for a detuning of 2.99(4) MHz yielding a coherence time $T^*_{2(e)} = 0.6(1)$ μs in good agreement with the coherence time of MW1 as expected.

photons, emphasizing the use of proximal nuclear spins as nuclear-spin memories.

5. Coherent control of the electron spin

For completeness, we show coherent control of the electron spin. In order to drive an electronic transition MW1 (MW2), we initialize into one of the four substates via pumping A1 and MW1 (MW2) followed by the application of the wanted measurement sequence of MW1 (MW2). Readout is performed again by using the initialization sequence. For such low-strain emitters, the electron Rabi frequency is heavily quenched for a field aligned parallel to the SnV center axis [43].

We use an damped sine oscillation with an additional linear increase to fit the data shown in Figs. 16(a) and 16(b). We attribute the damping and increase in baseline by heating effects at this high microwave power in the gigahertz regime.

Nevertheless, we show coherent Rabi oscillations using the same superconducting waveguide and achieve Rabi frequencies up to 1.66(1) MHz at input powers of 14 dBm. To improve Rabi frequencies, a finite angle can be chosen [6,43] or slightly more strain induced [6,9,10]. The coherence time measured via Ramsey decay shows slightly worse values of 0.7(1) μs, compared to earlier work [6,10,15], but has also been observed before [9].

[1] H. J. Kimble, *The quantum internet*, Nature (London) **453**, 1023 (2008).
[2] C. Bradac, W. Gao, J. Forneris, M. E. Trusheim, and I. Aharonovich, *Quantum nanophotonics with group IV defects in diamond*, Nat. Commun. **10**, 5625 (2019).
[3] T. Schröder, M. E. Trusheim, M. Walsh, L. Li, J. Zheng, M. Schukraft, A. Sipahigil, R. E. Evans, D. D. Sukachev, C. T. Nguyen, J. L. Pacheco, R. M. Camacho, E. S. Bielejec, M. D. Lukin, and D. Englund, *Scalable focused ion beam creation of nearly lifetime-limited single quantum emitters in diamond nanostructures*, Nat. Commun. **8**, 15376 (2017).
[4] M. E. Trusheim *et al.*, *Transform-limited photons from a coherent tin-vacancy spin in diamond*, Phys. Rev. Lett. **124**, 023602 (2020).
[5] J. Görlitz, D. Herrmann, P. Fuchs, T. Iwasaki, T. Taniguchi, D. Rogalla, D. Hardeman, P.-O. Colard, M. Markham, M. Hatano, and C. Becher, *Coherence of a charge stabilised tin-vacancy spin in diamond*, npj Quantum Inf. **8**, 45 (2022).
[6] I. Karapatzakis, J. Resch, M. Schrodin, P. Fuchs, M. Kieschnick, J. Heupel, L. Kussi, C. Sürgers, C. Popov, J. Meijer, C. Becher, W. Wernsdorfer, and D. Hunger, *Microwave control of the tin-vacancy spin qubit in diamond with a superconducting waveguide*, Phys. Rev. X **14**, 031036 (2024).
[7] D. D. Sukachev, A. Sipahigil, C. T. Nguyen, M. K. Bhaskar, R. E. Evans, F. Jelezko, and M. D. Lukin, *Silicon-vacancy spin qubit in diamond: A quantum memory exceeding 10 ms with single-shot state readout*, Phys. Rev. Lett. **119**, 223602 (2017).
[8] P.-J. Stas, Y. Q. Huan, B. Machielse, E. N. Knall, A. Suleymanzade, B. Pingault, M. Sutula, S. W. Ding, C. M. Knaut, D. R. Assumpcao, Y.-C. Wei, M. K. Bhaskar, R. Riedinger, D. D. Sukachev, H. Park, M. Lončar, D. S. Levonian, and M. D. Lukin, *Robust multi-qubit quantum network node with integrated error detection*, Science **378**, 557 (2022).
[9] E. I. Rosenthal, C. P. Anderson, H. C. Kleidermacher, A. J. Stein, H. Lee, J. Grzesik, G. Scuri, A. E. Rugar, D. Riedel, S. Aghaeimeibodi, G. H. Ahn, K. Van Gasse, and J. Vučković, *Microwave spin control of a tin-vacancy qubit in diamond*, Phys. Rev. X **13**, 031022 (2023).
[10] X. Guo *et al.*, *Microwave-based quantum control and coherence protection of tin-vacancy spin qubits in a strain-tuned diamond-membrane heterostructure*, Phys. Rev. X **13**, 041037 (2023).
[11] C. Adambukulam, B. C. Johnson, A. Morello, and A. Laucht, *Hyperfine spectroscopy and fast, all-optical arbitrary state initialization and readout of a single, ten-level ^{73}Ge vacancy nuclear spin qudit in diamond*, Phys. Rev. Lett. **132**, 060603 (2024).
[12] I. B. W. Harris, I. Christen, S. M. Patomäki, H. Raniwala, M. Sirotin, M. Colangelo, K. C. Chen, C. Errando-Herranz, D. J. Starling, R. Murphy, K. Shtyrkova, O. Medeiros, M. E. Trusheim, K. K. Berggren, P. B. Dixon, and D. Englund, *High-fidelity control of a strongly coupled electro-nuclear spin-photon interface*, arXiv:2505.09267.
[13] C. T. Nguyen, D. D. Sukachev, M. K. Bhaskar, B. Machielse, D. S. Levonian, E. N. Knall, P. Stroganov, C. Chia, M. J. Burek, R. Riedinger, H. Park, M. Lončar, and M. D. Lukin, *An integrated nanophotonic quantum register*

based on silicon-vacancy spins in diamond, Phys. Rev. B **100**, 165428 (2019).

[14] N. Grimm, K. Senkalla, P. J. Vetter, J. Frey, P. Gundlapalli, T. Calarco, G. Genov, M. M. Müller, and F. Jelezko, *Coherent control of a long-lived nuclear memory spin in a germanium-vacancy multi-qubit node*, Phys. Rev. Lett. **134**, 043603 (2025).

[15] H. K. C. Beukers, C. Waas, M. Pasini, H. B. van Ommen, Z. Ademi, M. Iuliano, N. Codreanu, J. M. Brevoord, T. Turan, T. H. Taminiau, and R. Hanson, *Control of solid-state nuclear spin qubits using an electron spin*-1/2, Phys. Rev. X **15**, 021011 (2025).

[16] M. Klotz, A. Tangemann, D. Opferkuch, and A. Kubanek, *Bipartite entanglement in a nuclear spin register mediated by a quasi-free electron spin*, arXiv:2508.05255.

[17] E. I. Rosenthal, S. Biswas, G. Scuri, H. Lee, A. J. Stein, H. C. Kleidermacher, J. Grzesik, A. E. Rugar, S. Aghaeimeibodi, D. Riedel, M. Titze, E. S. Bielejec, J. Choi, C. P. Anderson, and J. Vučković, *Single-shot readout and weak measurement of a tin-vacancy qubit in diamond*, Phys. Rev. X **14**, 041008 (2024).

[18] H. Bartling, J. Yun, K. Schymik, M. van Riggelen, L. Enthoven, H. van Ommen, M. Babaie, F. Sebastiano, M. Markham, D. Twitchen, and T. Taminiau, *Universal high-fidelity quantum gates for spin qubits in diamond*, Phys. Rev. Appl. **23**, 034052 (2025).

[19] J. M. Brevoord, L. De Santis, T. Yamamoto, M. Pasini, N. Codreanu, T. Turan, H. K. Beukers, C. Waas, and R. Hanson, *Heralded initialization of charge state and optical-transition frequency of diamond tin-vacancy centers*, Phys. Rev. Appl. **21**, 054047 (2024).

[20] Y. Herrmann, J. Fischer, J. M. Brevoord, C. Sauerzapf, L. G. C. Wienhoven, L. J. Feije, M. Pasini, M. Eschen, M. Ruf, M. J. Weaver, and R. Hanson, *Coherent coupling of a diamond tin-vacancy center to a tunable open microcavity*, Phys. Rev. X **14**, 041013 (2024).

[21] G. Thiering and A. Gali, *Ab initio magneto-optical spectrum of group-iv vacancy color centers in diamond*, Phys. Rev. X **8**, 021063 (2018).

[22] M. H. Metsch, K. Senkalla, B. Tratzmiller, J. Scheuer, M. Kern, J. Achard, A. Tallaire, M. B. Plenio, P. Siyushev, and F. Jelezko, *Initialization and readout of nuclear spins via a negatively charged silicon-vacancy center in diamond*, Phys. Rev. Lett. **122**, 190503 (2019).

[23] R. Kuate Defo, E. Kaxiras, and S. L. Richardson, *Calculating the hyperfine tensors for group-iv impurity-vacancy centers in diamond using hybrid density functional theory*, Phys. Rev. B **104**, 075158 (2021).

[24] T. Koch, C. Godfrin, V. Adam, J. Ferrero, D. Schroller, N. Glaeser, S. Kubicek, R. Li, R. Loo, S. Massar, G. Simion, D. Wan, K. De Greve, and W. Wernsdorfer, *Industrial 300 mm wafer processed spin qubits in natural silicon/silicon-germanium*, npj Quantum Inf. **11**, 59 (2025).

[25] E. Magesan, J. M. Gambetta, and J. Emerson, *Characterizing quantum gates via randomized benchmarking*, Phys. Rev. A **85**, 042311 (2012).

[26] Z.-H. Wang, G. de Lange, D. Ristè, R. Hanson, and V. V. Dobrovitski, *Comparison of dynamical decoupling protocols for a nitrogen-vacancy center in diamond*, Phys. Rev. B **85**, 155204 (2012).

[27] K. Senkalla, G. Genov, M. H. Metsch, P. Siyushev, and F. Jelezko, *Germanium vacancy in diamond quantum memory exceeding 20 ms*, Phys. Rev. Lett. **132**, 026901 (2024).

[28] R. de Sousa, *Electron spin as a spectrometer of nuclear-spin noise and other fluctuations*, in *Electron Spin Resonance and Related Phenomena in Low-Dimensional Structures*, edited by M. Fanciulli (Springer, Berlin, Heidelberg, 2009), pp. 183–220.

[29] J. Resch, I. Karapatzakis, and M. Elshorbagy, Dataset belonging to the publication "High-Fidelity Control of a 13C Nuclear Spin Coupled to a Tin-Vacancy Center in Diamond." Karlsruhe Institute of Technology (2026), 10.35097/c00su4fewkzanfgh.

[30] J. Heupel, M. Pallmann, J. Körber, D. Hunger, J. P. Reithmaier, and C. Popov, *Fabrication of high-quality thin single-crystal diamond membranes with low surface roughness*, Phys. Status Solidi (a) **220**, 2200465 (2023).

[31] J. Görlitz, D. Herrmann, G. Thiering, P. Fuchs, M. Gandil, T. Iwasaki, T. Taniguchi, M. Kieschnick, J. Meijer, M. Hatano, A. Gali, and C. Becher, *Spectroscopic investigations of negatively charged tin-vacancy centres in diamond*, New J. Phys. **22**, 013048 (2020).

[32] R. N. Simons, *Coplanar Waveguide Circuits, Components, and Systems* (John Wiley & Sons, New York, 2004).

[33] L. Childress and J. McIntyre, *Multifrequency spin resonance in diamond*, Phys. Rev. A **82**, 033839 (2010).

[34] J. Meinel, V. Vorobyov, and B. u. Yavkin, *Heterodyne sensing of microwaves with a quantum sensor*, Nat. Commun. **12**, 2737 (2021).

[35] M. Newville, R. Otten, A. Nelson, T. Stensitzki, A. Ingargiola, D. Allan, A. Fox, F. Carter, and M. Rawlik, *Lmfit: Non-linear least-squares minimization and curve-fitting for Python* (2025), 10.5281/zenodo.15014437.

[36] M. H. Appel, A. Tiranov, A. Javadi, M. C. Löbl, Y. Wang, S. Scholz, A. D. Wieck, A. Ludwig, R. J. Warburton, and P. Lodahl, *Coherent spin-photon interface with waveguide induced cycling transitions*, Phys. Rev. Lett. **126**, 013602 (2021).

[37] C. J. Foot, *Atomic Physics*, Oxford Master Series in Physics (Oxford University Press, Oxford, 2005), Vol. 7.

[38] B. Smeltzer, J. McIntyre, and L. Childress, *Robust control of individual nuclear spins in diamond*, Phys. Rev. A **80**, 050302 (2009).

[39] L. Childress, M. V. G. Dutt, J. M. Taylor, A. S. Zibrov, F. Jelezko, J. Wrachtrup, P. R. Hemmer, and M. D. Lukin, *Coherent dynamics of coupled electron and nuclear spin qubits in diamond*, Science **314**, 281 (2006).

[40] A. Ulanowski, O. Kuijpers, B. Merkel, A. Holzäpfel, and A. Reiserer, *Cavity-enhanced spectroscopy of individual nuclear spins in a dense bath*, PRX Quantum **6**, 020344 (2025).

[41] P. Gundlapalli, P. J. Vetter, G. Genov, M. Olney-Fraser, P. Wang, M. M. Müller, K. Senkalla, and F. Jelezko,

High-fidelity single-shot readout and selective nuclear spin control for a spin-1/2 quantum register in diamond, arXiv:2510.09164.

[42] N. Codreanu, T. Turan, D. B. Rodriguez, M. Pasini, L. de Santis, M. Ruf, C. F. Primavera, L. G. C. Wienhoven, C. E. Smulders, S. Gröblacher, and R. Hanson, *Above-unity coherent cooperativity of tin-vacancy centers in diamond photonic crystal cavities*, arXiv:2511.13375.

[43] G. Pieplow, M. Belhassen, and T. Schröder, *Efficient microwave spin control of negatively charged group-iv color centers in diamond*, Phys. Rev. B **109**, 115409 (2024).